

The three-dimensional magnetohydrodynamics of ac helicity injection in the reversed field pinch

F. Ebrahimi,^{a)} S. C. Prager, J. S. Sarff, and J. C. Wright
University of Wisconsin-Madison, Madison, Wisconsin 53706

(Received 15 October 2002; accepted 2 January 2003)

ac magnetic helicity injection (also known as oscillating field current drive, OFCD) has been proposed as a technique to sustain the plasma current in a reversed field pinch. The three-dimensional, resistive magnetohydrodynamics computation is employed to examine the full nonlinear dynamics of OFCD, including the behavior of plasma fluctuations and instabilities. The three-dimensional results are also compared with one-dimensional classical and relaxed-state modeling. In OFCD, helicity is injected by oscillating the toroidal and poloidal surface loop voltages. This technique is able to sustain the plasma current, with the edge current mainly driven directly by the OFCD-generated fields, and the core current driven by plasma fluctuations. Fluctuations increase with OFCD, although the increase is concentrated mainly in one global, nearly ideal, mode. © 2003 American Institute of Physics. [DOI: 10.1063/1.1555622]

I. INTRODUCTION

Steady sustainment of the current in toroidal plasmas remains a challenge. For plasmas in which the current distribution relaxes by internal processes, various techniques known as magnetic helicity injection have been suggested for current sustainment. In such techniques, the resistive dissipation of magnetic helicity (and plasma current) is balanced by helicity injection, typically provided by voltages applied at the plasma surface. Internal relaxation processes are expected to enable current penetration to the core. In the present paper, we examine the detailed dynamics of ac helicity injection in the reversed field pinch (RFP), investigating both the effectiveness of the current drive and the response of the fluctuations in the plasma.

Magnetic helicity, K , is a measure of the knottedness of the magnetic field lines, and is defined as

$$K = \int \mathbf{A} \cdot \mathbf{B} \, dv - \phi_p \phi_z, \quad (1)$$

where \mathbf{A} is the magnetic vector potential and the integral extends over the plasma volume. The second term represents the linkage of toroidal flux within the plasma (ϕ_z) with poloidal flux (ϕ_p) that passes through the center of the torus. The second term is subtracted from the volume integral, as required to maintain gauge invariance.¹⁻³ The rate of change of helicity for a resistive magnetohydrodynamic (MHD) plasma is

$$\frac{\partial K}{\partial t} = 2 \phi_z v_z - 2 \int \Phi \mathbf{B} \cdot d\mathbf{s} - 2 \int \mathbf{E} \cdot \mathbf{B} \, dv, \quad (2)$$

where Φ is the electrostatic potential on the plasma surface and v_z is the toroidal loop voltage. Any technique to sustain the plasma current must also maintain helicity constant in time. In the usual toroidal induction, as in a tokamak, helicity dissipation is balanced by the dc toroidal loop voltage

present in the first term on the right-hand side. In dc electrostatic helicity injection helicity is maintained by the second term, which represents the intersection of a field line with a surface held at a constant electric potential. Electrostatic helicity injection has been studied experimentally in spheromaks⁴ and spherical tokamaks.⁵⁻⁷

In ac helicity injection the helicity is provided by oscillating fields in the first term. In steady state,

$$\overline{\phi_z \hat{v}_z} = \eta \overline{\int \mathbf{J} \cdot \mathbf{B} \, dv}, \quad (3)$$

where the overbar denotes a time average over a cycle of the oscillating fields, $\hat{\phi}_z$ and \hat{v}_z (the “hat” denotes an oscillating quantity). The oscillation in the poloidal flux is provided by an oscillating surface toroidal loop voltage. Hence, if toroidal and poloidal surface voltages are oscillated, with a 90 degree phase difference, then helicity is injected steadily, even in the absence of a dc loop voltage. This technique was suggested by Bevir and Gray¹ to sustain the current in an RFP. It has also been referred to as $F - \Theta$ pumping or oscillating field current drive (OFCD). We will here use the acronym OFCD. The technique was shown to demonstrate a small amount of current (about 5% of the total) in the ZT40-M RFP,⁸ with a phase dependence in agreement with theory. However, plasma-wall interactions generated by the oscillating plasma position precluded tests with larger voltages.

Considerations of helicity balance provide little information on the dynamics of the current drive. A somewhat more complete view is obtained through examination of the effect of the applied voltages on the fields within the plasma, using the mean-field parallel (to the cycle-averaged mean magnetic field) Ohm’s law,

$$\overline{(\mathbf{V}_{00} \times \mathbf{B}_{00})_{\parallel}} + \langle \tilde{\mathbf{V}} \times \tilde{\mathbf{B}} \rangle_{\parallel} = \overline{\eta \mathbf{J}_{\parallel}}, \quad (4)$$

where \mathbf{V}_{00} and \mathbf{B}_{00} are the oscillating velocity and magnetic fields with poloidal and toroidal mode numbers $m = n = 0$, $\tilde{\mathbf{V}}$

^{a)}Electronic mail: febrahimi@wisc.edu

and $\bar{\mathbf{B}}$ are the fields with $m, n \neq 0$, and $\langle \rangle$ denotes an average over a magnetic surface [$\langle \cdot \rangle_{\parallel} = \langle \cdot \rangle \cdot \bar{\mathbf{B}}/B$, where $\bar{\mathbf{B}}$ is the cycle-averaged mean (0,0) magnetic field]. We see that there are two dynamo-like current drive terms on the left-hand side, one arising from the one-dimensional oscillating fields that occur at the OFCD frequency (the first term) and one that arises from nonaxisymmetric plasma fluctuations and instabilities (the second term). In the absence of fluctuations (neglecting the second term), a current is driven by the symmetric, oscillating fields. The oscillating radial velocity combines with the oscillating magnetic field to produce a dc current. This current is confined to within a classical resistive skin depth near the plasma surface, and decays to zero at the plasma center. It is a classical effect, although one that is absent in a plasma without flow. Considering that $\mathbf{V}_{00} = \mathbf{E}_{00} \times \mathbf{B}/B^2$, the first term can also be written as $(\mathbf{E}_{00} \cdot \mathbf{B}_{00})/B$. Hence, the classical OFCD effect can also be viewed as a time-averaged parallel component of the oscillating electric field.

The OFCD technique relies upon magnetic fluctuations to relax the current density profile. Fluctuations are generated by the OFCD-driven edge current (the first term on the LHS), that then generate current in the plasma core via the second term, the MHD dynamo. The original studies of OFCD assumed that the plasma relaxes to a Taylor state⁹ with J_{\parallel}/B spatially constant.¹⁰ MHD computation in which the fluctuations are treated as a hyperresistivity has been used to treat the 1D behavior of the plasma with OFCD.^{11,12} Three-dimensional MHD computation has been used to study spheromak formation by helicity injection¹³ and to model electrostatic helicity injection in tokamaks.¹⁴ The implications for transport associated with helicity injection have also been investigated.^{15,16}

In this paper we employ three-dimensional, resistive MHD computation to study the nonlinear dynamics of OFCD. This permits us to address two key questions: what is the effectiveness of OFCD as a current drive technique and what is its effect on plasma fluctuations? The basic equations are introduced in Sec. II. The classical OFCD effect, which occurs in the absence of fluctuations, is calculated in Sec. III, both through 1D computation and analytic quasilinear calculation. This calculation provides a benchmark to which the additive effect of the fluctuations can be compared. The effect of the fluctuations is considered first through a 1D relaxed state model, in which the effect of fluctuations is represented through an assumption that the plasma maintains a preferred J_{\parallel}/B profile. This calculation (Sec. IV) provides predictions, including scaling of key quantities with Lundquist number, that can also be compared to the 3D computation. The full 3D results are presented in Sec. V, for Lundquist numbers of 10^5 and 5×10^5 . Investigation of the cycle-averaged quantities reveals that the plasma current (and helicity) can indeed be sustained by OFCD. Examination of the surface-averaged quantities throughout a cycle indicates that the plasma current oscillates substantially, although the magnitude of the oscillation decreases with Lundquist number. Plasma fluctuations increase significantly with OFCD; however the increase is concentrated mainly in

a global mode that is nearly ideal (resonant at the extreme plasma edge). The core-resonant tearing modes are not increased significantly. We summarize in Sec. VI.

II. BASIC EQUATIONS

To understand the dynamics of OFCD both the tearing fluctuations and the oscillation of the mean quantities should be studied. Therefore, we model OFCD using both 1D and 3D computations. We employ the 3D resistive MHD code, DEBS,¹⁷ to solve the compressible resistive MHD equations in periodic cylindrical geometry,

$$\begin{aligned} \frac{\partial \mathbf{A}}{\partial t} &= S \mathbf{V} \times \mathbf{B} - \eta \mathbf{J}, \\ \rho \frac{\partial \mathbf{V}}{\partial t} &= -S \rho \mathbf{V} \cdot \nabla \mathbf{V} + S \mathbf{J} \times \mathbf{B} + \nu \nabla^2 \mathbf{V}, \end{aligned} \quad (5)$$

$$\mathbf{B} = \nabla \times \mathbf{A}, \quad \mathbf{J} = \nabla \times \mathbf{B},$$

where time and radius are normalized to the resistive diffusion time $\tau_R = 4 \pi a^2 / c^2 \eta_0$ and the minor radius a , velocity to the Alfvén velocity V_A , and magnetic field \mathbf{B} to the magnetic field on axis B_0 . $S = \tau_R / \tau_A$ is the Lundquist number (where $\tau_A = a / V_A$), and ν is the viscosity coefficient, which measures the ratio of characteristic viscosity to resistivity (the magnetic Prandtl number). The mass density ρ is assumed to be uniform in space and time. The resistivity profile has been chosen to resemble the experimental profiles (increasing near the plasma edge), $\eta = (1 + 9(r/a)^{20})^2$. Oscillating axial and azimuthal electric fields are imposed at the wall, $\hat{E}_z = \varepsilon_z \sin(\omega t)$, $\hat{E}_\theta = \varepsilon_\theta \sin(\omega t + \pi/2)$, where ε_z and ε_θ are the axial and azimuthal ac amplitudes, respectively. The oscillation period is required to be long compared to the plasma relaxation time (the hybrid tearing time scale $\tau_{\text{hybrid}} \sim \sqrt{\tau_R \tau_A}$), and short compared to resistive diffusion time τ_R ($\tau_{\text{hybrid}} < \tau_\omega < \tau_R$).^{11,12}

III. ONE-DIMENSIONAL CLASSICAL PLASMAS

One-dimensional studies, in which all quantities depend on radius only, are executed to examine plasma behavior with OFCD, but in the absence of nonsymmetric MHD fluctuations. This allows us to evaluate the OFCD-driven current, concentrated in the outer region of the plasma, that occurs in the absence of MHD relaxation. The 1D calculations are useful for comparison to 3D computation to highlight the additive effect of relaxation. In Sec. III A we display computational solution to the 1D MHD equations; Sec. III B contains an analytic quasilinear treatment for a simple 1D equilibrium.

A. One-dimensional computations

We employ the DEBS code with all θ and z dependent fluctuations suppressed. To study the linear dynamic response of both the mean and oscillating fields, low oscillating field amplitudes have been imposed on a plasma that is initially current free ($B_\theta = 0$, $B_z = \text{constant}$). The time-averaged (over a cycle) magnetic field profiles in steady-state are shown in Fig. 1. The axial field is little affected by the

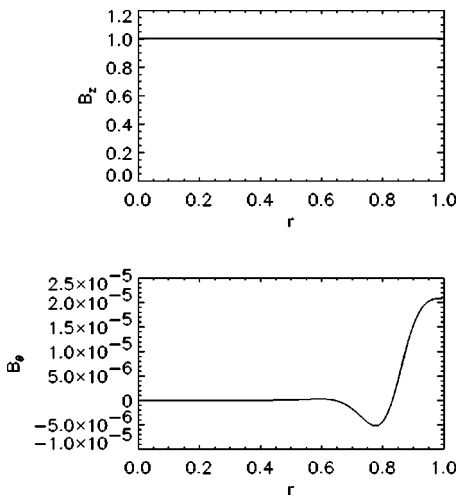


FIG. 1. Time-averaged profiles for axial and azimuthal magnetic fields, obtained in steady state from 1D computation ($\epsilon_z=1.0, \epsilon_\theta=0.1, \omega=600\tau_R^{-1}, S=10^5$).

small oscillating fields. The alteration in the azimuthal field results from the cycle-averaged current density, shown in Fig. 2(a). The current density is localized to the outer region of the plasma, penetrating a distance equal to the classical skin depth $\delta=(\eta/\omega)^{1/2}$. The time dependence of the current density throughout one cycle is shown in Fig. 2(b). The oscillatory current density is similar to the classical penetration

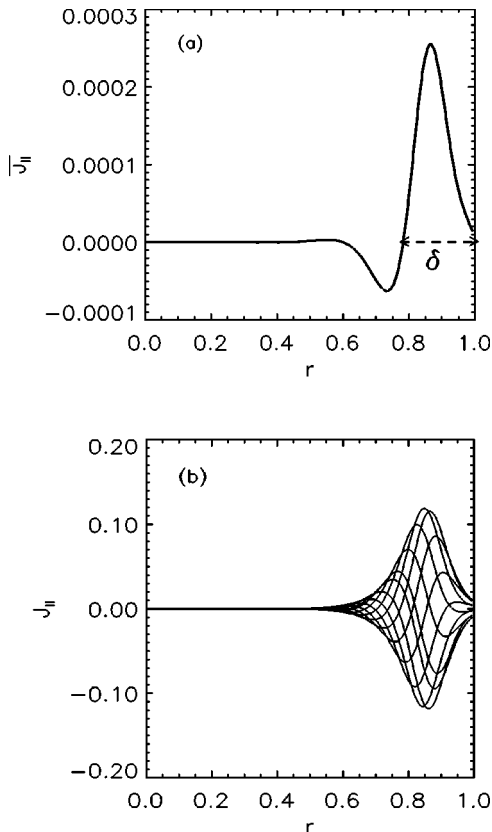


FIG. 2. Radial profiles of (a) cycle-averaged parallel current density, \bar{J}_\parallel . (b) Parallel current density at different times during one cycle (1D low amplitude computation).

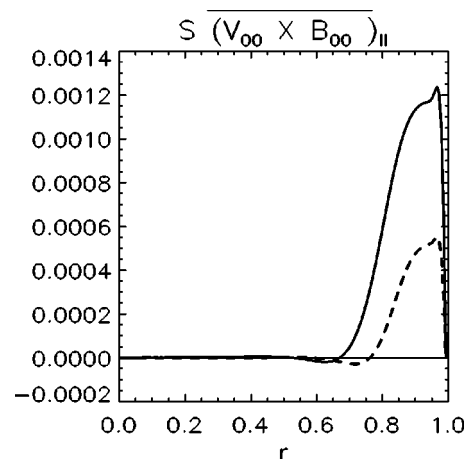


FIG. 3. Cycle-averaged dynamo-like term $\overline{(\mathbf{V}_{00} \times \mathbf{B}_{00})_\parallel}$ vs radius, for the 1D computation. The oscillation frequency ω is $200\tau_R^{-1}$ and $600\tau_R^{-1}$ for the solid and dashed lines, respectively. The solid line has three times higher helicity injection rate. For both cases $\hat{E}_z=1.0 \sin(\omega t)$, $\hat{E}_\theta=-0.1 \cos(\omega t)$, $S=10^5$.

that occurs for a solid metal. However, the cycle-averaged component arises from the cycle-averaged term $(\mathbf{V}_{00} \times \mathbf{B}_{00})_\parallel$, a dynamo-like effect due to the classically penetrating oscillatory fields, similar to that reported in Ref. 18. This effect is proportional to the helicity injection rate ($\sim \epsilon_z \epsilon_\theta / \omega$), as seen in Fig. 3.

At high oscillating field amplitudes (about 10 times larger), the oscillatory behavior of the fields change. The electric field contains both higher harmonics and subharmonics (low frequency) components, as seen in Figs. 4(a) and 4(b). The subharmonic component yields a nonzero cycle-averaged electric field that decays toward zero as the plasma approaches steady state. The cycle-averaged dynamo-like effect $(\mathbf{V}_{00} \times \mathbf{B}_{00})_\parallel$, increases with the helicity injection rate; however its structure remains unchanged (Fig. 5).

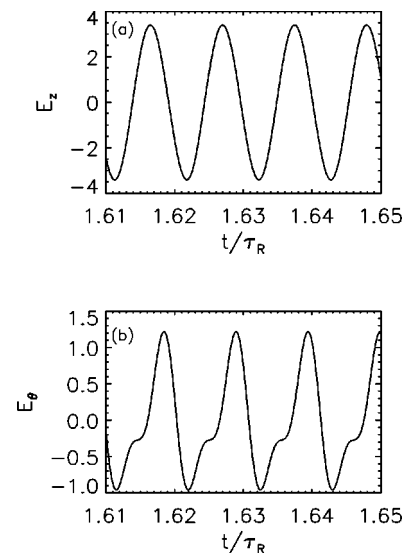


FIG. 4. (a) Axial and (b) azimuthal electric fields vs time at radius $r=0.89$, respectively.

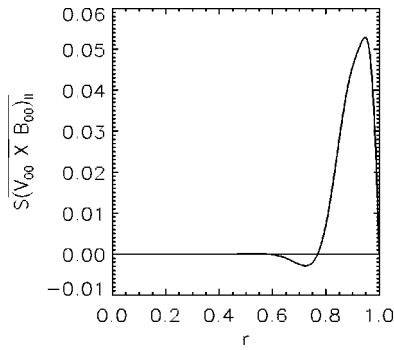


FIG. 5. Cycle-averaged dynamo effect $(\mathbf{V}_{00} \times \mathbf{B}_{00})_{||}$ for high driving amplitudes, 1D computation ($\epsilon_z = 10.0, \epsilon_\theta = 1.0, \omega = 600\tau_R^{-1}, S = 10^5$).

B. Analytical calculation and quasilinear effects

From the 1D computation, we see that low amplitude oscillating fields penetrate into the plasma with the OFCD frequency while both higher and lower frequencies are generated for higher amplitudes (large forcing amplitudes). To understand the time dependence of the fields, one-dimensional, linear, resistive MHD equations [Eq. (5)] are analytically solved in cylindrical geometry. The partial differential equations are solved for uniform magnetic field $\mathbf{B} = B_0 \hat{z}$, $\nabla p = 0$, no viscosity, with initial conditions $A_z^1(r, 0) = \text{const}$, $A_\theta^1(r, 0) = 0$ and boundary conditions $A_z^1(a, t) = (-\epsilon_{z0}/\omega)\cos(\omega t)$, $A_\theta^1(a, t) = (-\epsilon_{\theta0}/\omega)\sin(\omega t)$, where the “1” superscript denotes a linear oscillating quantity. The equations for the vector potential and velocity fields can be simplified as follows:

$$\frac{\partial \mathbf{A}^1}{\partial t} = \mathbf{V}^1 \times \mathbf{B} - \eta \nabla \times \nabla \times \mathbf{A}^1, \tag{6}$$

$$\rho \frac{\partial \mathbf{V}^1}{\partial t} = -\nabla(\mathbf{B} \cdot \mathbf{B}^1). \tag{7}$$

Equations (6) and (7) can be combined in the form of axial and azimuthal vector potential (A_z^1, A_θ^1),

$$\frac{\partial A_z^1}{\partial t} = \eta \left(\frac{\partial^2 A_z^1}{\partial r^2} + \frac{1}{r} \frac{\partial A_z^1}{\partial r} \right), \tag{8}$$

$$\begin{aligned} \frac{\partial^2 A_\theta^1}{\partial t^2} = & \frac{S^2 B_0^2}{\rho} \left[\frac{\partial^2 A_\theta^1}{\partial r^2} + \frac{1}{r} \frac{\partial A_\theta^1}{\partial r} - \frac{A_\theta^1}{r^2} \right] + \eta \frac{\partial}{\partial t} \left[\frac{\partial^2 A_\theta^1}{\partial r^2} \right. \\ & \left. + \frac{1}{r} \frac{\partial A_\theta^1}{\partial r} - \frac{A_\theta^1}{r^2} \right]. \end{aligned} \tag{9}$$

The normalization of the equations is similar to the one used in Sec. II. The partial differential equation (PDE) with nonhomogeneous boundary condition for the toroidal vector potential [Eq. (8)] represents a driven resistive diffusion equation. The PDE for the poloidal vector potential [Eq. (9)] consists of Alfvén waves and resistively damped modes. The Laplace transform method can be applied to Eqs. (8) and (9). The solution for A_z^1 and B_θ^1 can be written as an expansion of eigenfunctions (Bessel functions):

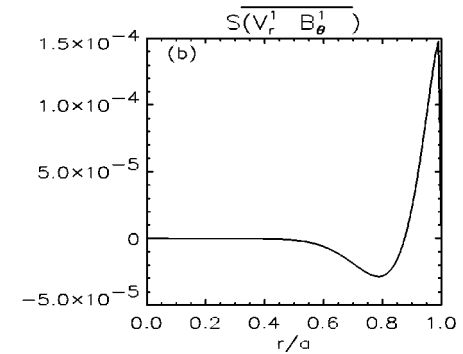
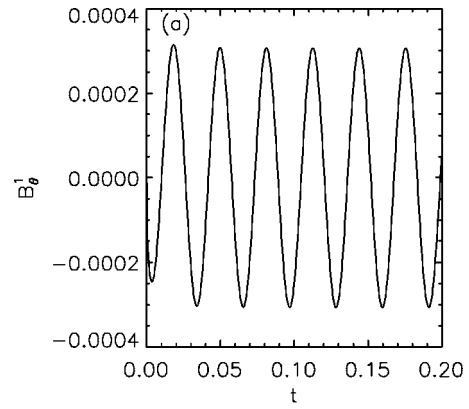


FIG. 6. (a) B_θ^1 vs time at radius $r/a = 0.8$ ($\epsilon_{z0} = 1.0, \epsilon_{\theta0} = 0.1, \omega = 200.0\tau_R^{-1}, S = 10^5$). (b) $S(\mathbf{V}_r^1 \mathbf{B}_\theta^1)$ vs radius calculated analytically in 1D for the same parameter in Fig. 3 (solid line).

$$A_z^1(r, t) = \frac{-\epsilon_{z0}}{\omega} \cos(\omega t) + \sum_{n=1}^{\infty} b_n(t) J_0(\lambda_n r),$$

$$B_\theta^1 = \sum_{n=1}^{\infty} \lambda_n b_n(t) J_1(\lambda_n r), \tag{10}$$

where

$$\begin{aligned} b_n(t) = & \alpha_n(\omega, \omega_n) [\omega_n \sin(\omega t) - \omega \cos(\omega t) \\ & + \omega \exp(-\omega_n t)], \end{aligned} \tag{11}$$

$$\alpha_n(\omega, \omega_n) = \frac{2\epsilon_{z0}}{\lambda_n \omega_n} \frac{1}{J_1(\lambda_n) (\omega^2 + (\omega_n)^2)},$$

$\omega_n = \eta \lambda_n^2$, and λ_n are the zeros of J_0 . Here, we have assumed uniform density and resistivity profiles ($\rho = \eta = 1$). The solution for B_θ^1 consists of an oscillating part at the OFCD frequency and a transient decaying part [Fig. 6(a)]. Equation (9) can be solved for A_θ^1 and subsequently for V_r^1 as follows:

$$V_r^1(r, t) = \sum_{m=1}^{\infty} C_m(t) \phi_m(r), \tag{12}$$

where

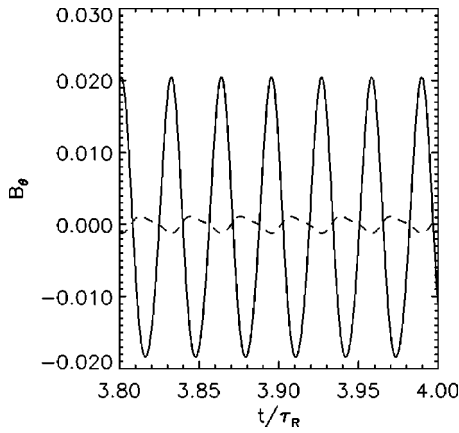


FIG. 7. B_θ at $r/a=0.65$ (dashed) and $r/a=0.94$ (solid) vs time, calculated numerically for the 1D model with the quasilinear term.

$$C_m(t) = \frac{2S\varepsilon_{\theta 0}}{(\omega^2 - \omega_m^2)} \left[\frac{-\omega_m \cos(\omega t)}{\omega} + \frac{\omega \cos(\omega_m t)}{\omega_m} \right],$$

$$\phi_m(r) = \frac{1}{J_1'(\lambda_m)} \left[\frac{\lambda_m^2}{4} (J_3(\lambda_m r) - 3J_1(\lambda_m r)) \right. \\ \left. + \frac{\lambda_m}{2r} (J_0(\lambda_m r) - J_2(\lambda_m r)) - \frac{J_1(\lambda_m r)}{r^2} \right], \quad (13)$$

$\omega_m = SB_0/\sqrt{\rho}\lambda_m$, and λ_m are the zeros of J_1 ($B_0 = \rho = 1$). The cycle-averaged ($V_r^1 \times B_\theta^1$) effect can be obtained from the analytical solutions, $V_r^1(r, t) \times B_\theta^1(r, t) = \sum_{m=1}^{\infty} C_m(t) \phi_m(r) \times \sum_{n=1}^{\infty} \lambda_n b_n(t) J_1(\lambda_n r)$. Figure 6(b) shows $S(V_r^1 B_\theta^1)$ from the analytical calculations, which agrees with the 1D computation (Fig. 3). The sharp edge feature in Fig. 6(b) results from the uniform resistivity profile assumed in the analytical model and the absence of viscosity. In the 1D computation of $(\mathbf{V}_{00} \times \mathbf{B}_{00})_\parallel$ (Sec. III A), the resistivity profile is exponential and the viscosity is finite. At high S , for arbitrary frequency and amplitudes, the second term $\cos(\omega_m t)$ in $C_m(t)$ [Eq. (13)] represents high frequency oscillations. These high frequency oscillations are also present in 1D computation (Sec. III A) for the field solutions but dissipate at finite viscosity, and also dissipate due to the fluctuations in 3D computation.

To understand the time response of the plasma to large oscillating amplitudes, the quasilinear effect is investigated including $f(r, t) = V_r^1(r, t) \times B_\theta^1(r, t)$, as an inhomogeneous source to the homogeneous PDE for A_z^1 . The 1D driven diffusion equation plus the quasilinear term is solved numerically using the Crank–Nicolson method. As shown in Fig. 7 the time response is a combination of the OFCD frequency, higher harmonics and a lower frequency which arises from the product of the exponential decaying component and the oscillation. The inhomogeneous solution can be found analytically as well, by defining $A_z^1(r, t) = \sum_{n=1}^{\infty} d_n(t) J_0(\lambda_n r)$, where now $d_n(t)$ has a different time dependence, which are the combination of the OFCD frequency, the harmonics, transient decaying solutions and the product of exponential decaying and the oscillations, $\sin(2\omega t)$, $\sin((\omega \pm \omega_m)t)$, $\sin(\omega t) \exp(-\omega_n t)$, $\exp(-\omega_n t)$.

Through the $\sin(\omega t) \exp(-\omega_n t)$ combinations in time, a nonzero time-averaged electric field is generated mainly at high amplitudes when the contribution of the quasilinear term becomes important. This electric field decays slowly on a resistive diffusion time scale. A nonzero mean electric field is similarly seen in large amplitude 1D computations (Sec. III A) as well as the nonlinear 3D computations below. However, this electric field becomes small as the plasma gets close to quasisteady state.

IV. ONE-DIMENSIONAL RELAXED-STATE PLASMA

Section III described the one-dimensional MHD plasma response to an applied oscillating electric field in the limit where the driven current diffuses classically. In this section we examine a different extreme, where turbulent diffusion maintains a relaxed-state current profile at every instant in time. The distinctive feature of a relaxed-state plasma is a stationary $\mu_0 \mathbf{J} \cdot \mathbf{B}/B^2 = \lambda_\parallel(r)$ profile shape, independent of varying electrical boundary conditions. Small-scale fluctuations are assumed to provide a turbulent emf in just the right amount at each radius to maintain this preferred $\lambda_\parallel(r)$ shape. The zero-pressure limit of a fully relaxed plasma with no residual magnetic free energy is well known to be $\lambda_\parallel(r) = \text{constant}$, as described by Taylor.⁹ However, for the discussion here, $\lambda_\parallel(r)$ can be any partially relaxed profile which is nonuniform in space but stationary in time (with finite residual magnetic free energy). Plasma pressure may also be included for more realistic modeling if the pressure evolution is easily described, such as a constant-beta assumption.

An experimental plasma operating with sufficiently strong relaxation has a stationary $\lambda_\parallel(r)$ profile when averaged over relaxation process cycling, but the shape is typically nonuniform. This behavior is also reproduced in 3D nonlinear MHD computation. Consequently relaxed-state modeling on time scales slow compared to the relaxation time $\tau_{\text{relax}} \sim \sqrt{S} \tau_A$ provides a way to predict plasma response to a prescribed electric field at the plasma surface, especially when time-consuming nonlinear, three-dimensional MHD computation is impractical or impossible. Particularly important is the high- S limit which remains a challenge for computational MHD, yet accessible in experimental plasmas. Relaxed state modeling also can be compared to the 3D computation.

We proceed in Sec. IV A with a description of the relaxed state evolution model, including an example simulation of OFCD sustainment. Section IV B covers the scaling of the OFCD-induced current and field modulation amplitudes for key parameters S , drive frequency ω , and the relative strengths of the axial and poloidal electric field amplitudes. Section IV C describes the time and space dependence of the implied dynamo emf required to maintain a relaxed-state current profile throughout an OFCD cycle, a prelude to Sec. V.

A. Model for relaxed-state evolution

Despite implications for a complex, nonlinear, three-dimensional evolution (the topic of Sec. V), relaxed-state

plasmas are easy to model because the mean current is prescribed. The instantaneous one-dimensional (mean-field) equilibrium is a solution of

$$\nabla \times \mathbf{B} = \lambda_{\parallel}(r, t) \mathbf{B} + \mathbf{B} \times \nabla p / B^2. \quad (14)$$

For a relaxed-state plasma, the λ_{\parallel} profile has a stationary shape, with the time and space dependencies separable as $\lambda_{\parallel}(r, t) = \lambda_0(t) \Lambda_{\parallel}(r)$. Only the amplitude varies in time in this model, specified by the value λ_0 at the magnetic axis ($r=0$). The profile shape $\Lambda_{\parallel}(r)$ is an input determined by theory or experimental behavior, for example, $\Lambda_{\parallel}(r) = 1$ for the fully relaxed state plasma. For results presented here, $\Lambda_{\parallel}(r) = 1 - (r/a)^4$ is chosen to mimic experimental RFP plasmas (in particular MST current profiles averaged over the sawtooth relaxation cycle). It also resembles the current profile obtained in 3D MHD computation. Finite diamagnetic current is straightforwardly included in relaxed-state modeling if the pressure evolution can be specified (e.g., constant-beta assumption). However, the zero-pressure limit is adopted here to permit direct comparison with results in Secs. II and V. Since $\beta \ll 1$, finite pressure typically introduces small changes and does not substantially impact OFCD solutions.

The evolution of a relaxed-state plasma is fully determined by a global magnetic energy balance, with the magnetic field profiles given by Eq. (14). From the Poynting theorem, the magnetic energy balance for the total plasma volume can be written as

$$v_z I_z - v_{\theta} I_{\theta} = \partial W / \partial t + P_{\Omega}, \quad (15)$$

where I_z is the axial (toroidal) plasma current, I_{θ} is the poloidal current in the axial field magnet surrounding the plasma, v_z and v_{θ} are the one-turn axial and poloidal loop voltages at the plasma surface respectively, $\partial W / \partial t$ is the rate-of-change of the magnetic (plus generally thermal) energy within the plasma volume, and P_{Ω} is the Ohmic dissipation within the plasma volume. Equation (15) resembles the description of power flow in an electrical circuit, hence this type of modeling is often dubbed zero dimensional. Nevertheless, a complete one-dimensional evolution of the plasma is described by Eqs. (14) and (15) with $\lambda_{\parallel}(r, t) = \lambda_0(t) \Lambda_{\parallel}(r)$, given specified values for $v_z(t)$ and $v_{\theta}(t)$. With the normalizations described in Sec. II (except for time, normalized instead to τ_A), Eq. (15) can be written in dimensionless form as

$$\frac{\partial W}{\partial \lambda_0} \frac{\partial \lambda_0}{\partial t} = 2 \phi_z \left(\frac{a}{R} \Theta v_z - F v_{\theta} \right) - S^{-1} P_{\Omega}, \quad (16)$$

where $\Theta = \mu_0 a I_z / 2 \phi_z$ and $F = \mu_0 R I_{\theta} / 2 \phi_z$ are the pinch and reversal values, respectively, commonly used normalizations of the axial and poloidal current. The axial magnetic flux is ϕ_z . Dimensionless W , $\partial W / \partial \lambda_0$, F and Θ are functions only of λ_0 and the specified $\Lambda_{\parallel}(r)$. P_{Ω} is additionally a function of the normalized resistivity profile, assumed stationary in this model. For comparison with the results in Secs. II and V, the same resistivity profile $\eta(r) = \eta(0) [1 + 9(r/a)^{20}]^2$ is used.

To create an OFCD simulation, the drive frequency, amplitudes, and relative phase of the loop voltages (set for

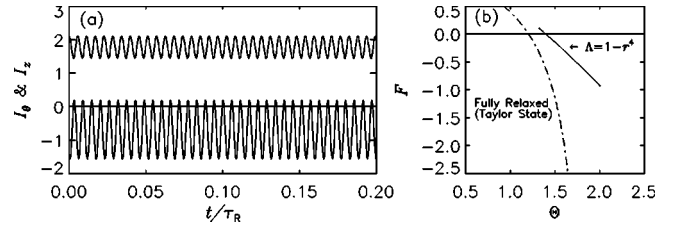


FIG. 8. (a) Axial and poloidal currents for an OFCD-sustained relaxed-state plasma with $S = 5 \times 10^5$, $\omega = 2.85 \times 10^3 \tau_A$, $R/a = 1.66$, and relative loop voltage amplitudes $\hat{v}_z = 14.5 \hat{v}_{\theta}$. The $F - \Theta$ trajectory is shown in (b) relative to fully relaxed equilibria, for which $\Lambda = 1$ (dotted-dashed line). The parameters for this relaxed-state case are identical to the high- S 3D MHD study in Sec. V B below, with the surface voltages adjusted to produce the same maximum $F = 0.1$. See Fig. 32.

maximum helicity injection) must be specified, as well as dimensionless parameters S and R/a (cylinder length $= 2\pi R$). Keeping in mind that $v_{\theta} = -\partial \phi_z / \partial t$, Eq. (16) is easily solved for $\lambda_0(t)$, from which the magnetic equilibrium evolution follows. For results here, fourth-order Runge–Kutta integration with 100 time steps per OFCD period is used to time-advance the solution.

In stark contrast to the results in the preceding section, OFCD sustainment of a dc current with relatively small superposed ac modulation occurs when the plasma maintains a relaxed state, as illustrated in Fig. 8(a). This relaxed-state simulation has the same set of parameters used in the $S = 5 \times 10^5$ 3D nonlinear MHD simulations described in Sec. V B below (see Fig. 32 for reference). The peak-to-peak axial current modulation is $\sim 30\%$, while the poloidal current modulation is yet larger. The $F - \Theta$ trajectory during an OFCD cycle is shown in Fig. 8(b). This trajectory is constrained to a well-defined curve unique to the choice of $\Lambda_{\parallel}(r)$. The 3D simulations in Sec. V display somewhat larger ac modulation amplitude and a more complicated $F - \Theta$ limit cycle that circles near the relaxed-state curve. The frequency for this set of parameters is probably near the maximum allowable relative to the relaxation time scale ($\omega \sqrt{\tau_R \tau_A} = 1.56$).

The data presented in the next section describe the scaling of the ac modulation amplitude. These data were collected from relaxed-state simulations similar to that shown in Fig. 8 but with parameters varied to expose the parameter dependence. In each simulation the surface loop voltage amplitudes are adjusted to produce a constant time-average axial current and a specified maximum value for the reversal parameter during the OFCD cycle (usually $F = -0.1$).

B. Scaling of the ac modulation amplitudes

In order for OFCD to have practical value, it is necessary that the ac modulation amplitudes of the currents be relatively small. It is therefore important to understand how the modulation amplitudes vary with Lundquist number S , the drive frequency ω , aspect ratio R/a , and the relative amplitudes of the axial and poloidal loop voltages. For relaxed-state modeling, the scaling of the modulation amplitudes with these parameters is straightforwardly obtained by varying each individually, holding the others fixed. The re-

sults of this scaling analysis are reported in this section. The ac modulation that occurs for a relaxed-state plasma probably represents the lower bound for any real plasma. In Sec. V below, 3D nonlinear MHD analysis demonstrates OFCD with modulation amplitude larger than for a relaxed state, but not grossly larger. Most importantly, sufficient relaxation occurs in the 3D analysis. This is not an obvious outcome and bolsters reliability in the scaling predictions from much simpler relaxed-state modeling.

The scaling of the axial current modulation is largely controlled by the plasma’s unavoidable inductive reaction to an oscillating electric field. The axial loop voltage required for OFCD is substantially larger than the resistive dc voltage which would sustain the same time-average current. From an Ohm’s law perspective, the voltage is dominantly inductive $v_z \approx L dI_z/dt$. Since the (toroidal) inductance $L \approx \mu_0 R$, the relationship between the ac amplitude of the axial current, \hat{I}_z , and the applied axial loop voltage amplitude, \hat{v}_z , is roughly $\hat{v}_z \approx \mu_0 R \omega \hat{I}_z$ (the “hat” refers to the ac amplitude). A simple prediction for the scaling of the axial current modulation \hat{I}_z is formed by inserting the inductive response estimate for the loop voltage into a helicity balance. Equating the time-average ac helicity injection rate in OFCD to the steady-induction helicity injection rate yields

$$\frac{\hat{v}_z \hat{v}_\theta}{2\omega} = v_\Omega \hat{\phi}_z = \frac{\eta(0)R}{a^2} f_\Omega \bar{I}_z \bar{\phi}_z, \quad (17)$$

where v_Ω is the steady-induction (resistive) loop voltage and f_Ω is a form factor for the plasma resistance, essentially constant in this analysis. The overbar indicates a time-average (i.e., cycle-average) mean value. Inserting $\hat{v}_z = \mu_0 R \omega \hat{I}_z$ and defining $\xi = \hat{v}_z / \hat{v}_\theta$,

$$\left(\frac{\hat{I}_z}{\bar{I}_z}\right)^2 \approx \frac{f_\Omega}{\bar{\Theta}} \xi \frac{a}{R} \frac{1}{\omega \tau_R}. \quad (18)$$

The frequency is best normalized to the hybrid time $\omega \sqrt{\tau_A \tau_R} = \Omega_{\text{mhd}}$, with $\Omega_{\text{mhd}} < 1$ the expected upper bound requirement to permit sufficient relaxation over an OFCD cycle. By these simple arguments, the fractional ac modulation amplitude is predicted to scale as

$$\hat{I}_z / \bar{I}_z \sim S^{-1/4} \Omega_{\text{mhd}}^{-1/2} \xi^{1/2} (R/a)^{-1/2}. \quad (19)$$

A similar argument for the poloidal current modulation is not easily identified, although its scaling is equally important. For example, (empirically) the loss of axial field reversal typically causes an RFP plasma to become unstable and must be avoided in operation.

The scaling of the modulation amplitudes with the loop voltage ratio ξ is shown in Fig. 9. The data points represent a set of OFCD simulations, each with constant time-average current (but slightly different values). All of the key parameters are the same in each simulation, except for ξ . The fixed parameter values are listed in the figure caption. Since the poloidal current modulation varies considerably, the amplitudes of the loop voltages are adjusted in each simulation to keep the maximum value of $F = -0.1$. This guarantees the simulation has a reversed axial field at all times, as close as

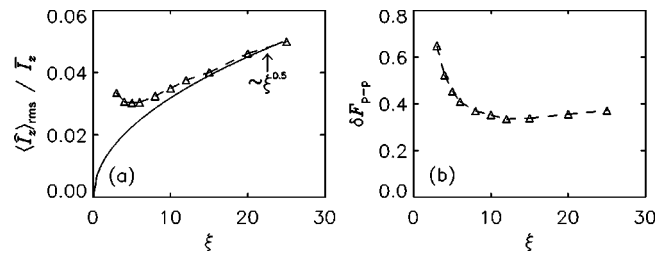


FIG. 9. Amplitudes of the (a) fractional rms axial current modulation and (b) peak-to-peak reversal parameter F modulation for varying oscillator amplitude ratio $\xi = \hat{v}_z / \hat{v}_\theta$. Fixed parameters are $S = 5 \times 10^7$, $\Omega_{\text{mhd}} = 1$, and $R/a = 3$. Note minimum δF_{p-p} at $\xi \sim 10$.

possible to normal experimental RFP conditions. This general procedure is repeated below, varying the other parameters.

Although the axial current modulation approaches the expected $\xi^{1/2}$ dependence only at large ξ in Fig. 9(a), this scaling is shown first because the poloidal current modulation—represented by the F modulation in Fig. 9(b)—is minimum at $\xi \sim 10$, increasing rapidly at lower ξ . Small ξ (or large ε_θ) corresponds to a large driven toroidal field modulation. To help maintain axial field reversal, $\xi = 10$ is chosen as the optimal loop voltage ratio. The sharp increase in the poloidal current modulation at small ξ probably spoils the $\xi^{1/2}$ scaling in the axial current modulation; coupling between the axial and poloidal fields is not accounted for in the derivation of Eq. (19).

The scaling of the axial current modulation with Lundquist number, S , is shown in Fig. 10(a), which fits very well the expected $S^{-1/4}$ dependence, except at low S where the modulation amplitude is largest. If OFCD is compatible with plasma confinement requirements, the current modulation at fusion reactor parameters is only a few percent. For this reason, the TITAN RFP reactor studies¹⁹ employed OFCD for current sustainment. Whether or not the required relaxation turbulence adversely impacts energy confinement is a major uncertainty in the viability of OFCD for fusion application.

The poloidal current modulation dependence on S is shown in Fig. 10(b), again represented by F . The modulation increases sharply at low S , which probably defines the most severe constraint on successful demonstration of OFCD, both theoretically and experimentally. When the plasma resistance is high, the required voltage to sustain the current is

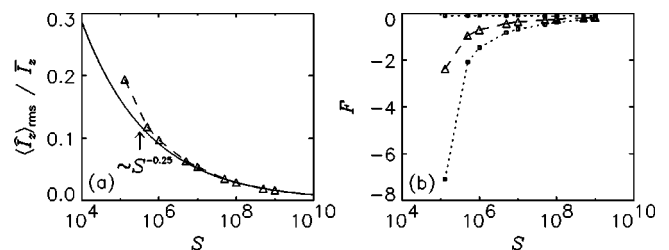


FIG. 10. (a) The fractional rms axial current modulation amplitude and (b) the reversal parameter variation as a function of S . Fixed parameters are $\xi = 10$, $\Omega_{\text{mhd}} = 1$, and $R/a = 3$. The triangles in (b) are the time-average mean- F , while the squares on dotted curves are the F -oscillation extremes. The loop voltages are adjusted to produce maximum $F = -0.1$ in all cases.

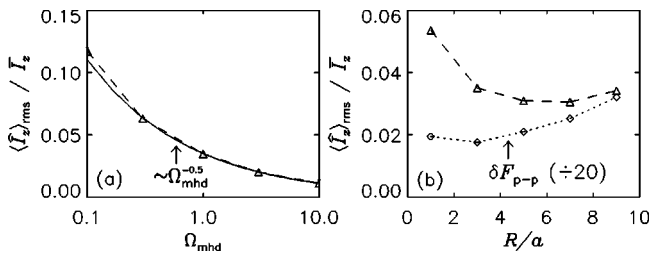


FIG. 11. The fractional rms axial current modulation for varying (a) frequency and (b) aspect ratio. Fixed parameters are $S=5 \times 10^7$, $\xi=10$, $R/a=3$ (for frequency scan), and $\Omega_{\text{mhd}}=1$ (for aspect ratio scan). The dotted curve in (b) is the peak-to-peak F -oscillation representing the poloidal current modulation ($\div 20$ only for illustration).

high, which in turn produces excessive poloidal current modulation, even for the optimal loop voltage ratio $\xi=10$ and maximum allowable frequency $\Omega_{\text{mhd}}=1$. Very little experimental RFP operation occurs with $|F|>1$. In practice, OFCD cannot be expected viable with $S \leq 10^6$, a relatively high limit. However, at reactor parameters, the poloidal current modulation is reasonable, and only now with the present generation of RFP experiments at $a \sim 0.5$ m and $S > 10^6$ can tests of total current sustainment by OFCD be contemplated.

The scaling of the modulation amplitudes with Ω_{mhd} and R/a are shown in Fig. 11. The frequency scaling is as expected, whereas the aspect ratio scaling is not. Coupling between the poloidal and axial fields most likely causes the scaling to diverge from $(R/a)^{-1/2}$, as with the ξ scaling. The toroidal and poloidal current modulation amplitudes increase and decrease together when changing S or Ω_{mhd} , hence their scalings are probably less sensitive to cross-field coupling.

C. Dynamo implications for an OFCD relaxed state

Although relaxed-state modeling does not provide a microscopic description of the relaxation mechanism, it does quantify the profile and time dependence of the emf required in Ohm's law to maintain a relaxed state. A comparison with steady induction provides insight into anticipated differences in the dynamo between OFCD and steady induction, the latter having a well-developed understanding in 3D nonlinear MHD.

To maintain a relaxed-state, in general parallel Ohm's law must include an emf, \mathcal{E}_{\parallel} , which balances the difference between the parallel inductive electric field and resistive drag

$$\eta J_{\parallel} - E_{\parallel} = \mathcal{E}_{\parallel}. \quad (20)$$

The detailed workings of \mathcal{E}_{\parallel} in 3D MHD is a topic in Sec. V below. In relaxed-state modeling, the radial profiles of $E_{\parallel} = (\mathbf{V}_{00} \times \mathbf{B}_{00})_{\parallel}$ and ηJ_{\parallel} are known, shown in Fig. 12(a) for both OFCD and steady induction. (The profiles are cycle averaged in the OFCD case.) The difference between these profiles implies \mathcal{E}_{\parallel} . Steady induction and OFCD require \mathcal{E}_{\parallel} with essentially opposite radial structure. In steady induction, most of the current is everywhere provided by the applied electric field except in the edge where the axial magnetic field is small. In OFCD, the time-average E_{\parallel} is zero at the magnetic axis (where $E_{\parallel} = E_z$) and maximum at the plasma surface. Consequently relaxation must support current in the

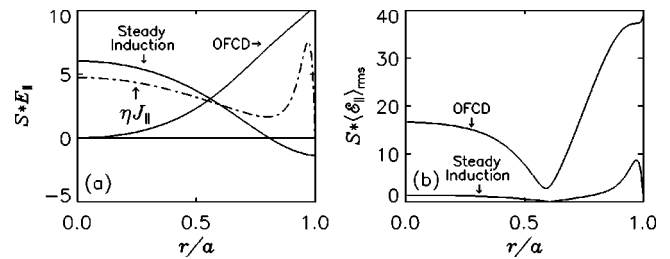


FIG. 12. (a) The parallel electric field profiles for OFCD (cycle averaged) and steady toroidal induction for the same parameters as in Fig. 8. The ηJ_{\parallel} profile (dotted-dashed curve) is identical for both types of current sustainment, i.e., the OFCD time-average current equals the steady-induction dc current in this comparison. The implied rms time-average dynamo profiles ($\mathcal{E}_{\parallel} = \eta J_{\parallel} - E_{\parallel}$) are shown in (b). For OFCD, the rms \mathcal{E}_{\parallel} is larger than its straight time-average since \mathcal{E}_{\parallel} oscillates with large positive-to-negative extremes.

core rather than the edge. Moreover, the mismatch between E_{\parallel} and ηJ_{\parallel} is larger in OFCD, as shown in Fig. 12(b). This is important because \mathcal{E}_{\parallel} is composed of turbulent quantities—specifically $\tilde{\mathbf{V}} \times \tilde{\mathbf{B}}$ in MHD—which can negatively impact plasma confinement. A larger $|\mathcal{E}_{\parallel}|$ implies larger fluctuation amplitudes. The S scaling of the fluctuation amplitudes is therefore critical in determining the consistency of relaxation and fusion plasma confinement. For steady induction, this scaling is not particularly optimistic in either experiment²⁰ or 3D MHD computation.^{21,22} In principle OFCD could scale differently, perhaps more favorably.

Hybrid current sustainment—combining partial steady induction with partial OFCD—provides an intriguing possibility for current profile control to minimize \mathcal{E}_{\parallel} . Steady induction would support the core current while OFCD would support the edge current. Relaxed-state modeling indicates the time-average \mathcal{E}_{\parallel} is minimal across the radius when the supplied power is roughly equally split between steady induction and OFCD. However, the rms \mathcal{E}_{\parallel} shown in Fig. 12(b) remains relatively large due to large positive-to-negative swings during the OFCD cycle. At two times in each cycle, the instantaneous magnitude of $|\mathcal{E}_{\parallel}|$ peaks at values up to ~ 5 – 10 times larger than the cycle-average \mathcal{E}_{\parallel} . This behavior stems from the large loop voltage which is dominantly inductive. Nevertheless hybrid sustainment will be interesting to investigate in 3D MHD where the detailed relaxation process could lessen these extremes.

V. THREE-DIMENSIONAL COMPUTATION

The complete dynamics of OFCD are studied using the 3D, nonlinear, resistive MHD DEBS code. In the 3D simulations the tearing fluctuations are present as well as the oscillations of the symmetric quantities. We employ an aspect ratio (cylinder length to radius divided by 2π) of 1.66. The number of dominant spatial Fourier modes in the RFP scales with aspect ratio ($n \sim 2R/a$). Hence, computation at low aspect ratio permits the essential physics to be explored while fewer Fourier modes need to be evolved.²³ We examine OFCD at two different Lundquist numbers, 10^5 and 5×10^5 . An assessment of OFCD requires information on scaling with Lundquist number; for example, it is expected that

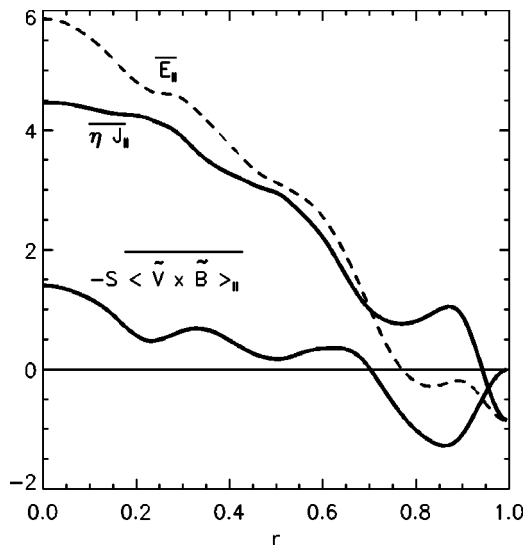


FIG. 13. Radial profiles of the three terms in parallel Ohm's law, $E_\parallel + S\langle \tilde{\mathbf{V}} \times \tilde{\mathbf{B}} \rangle_\parallel = \eta J_\parallel$ for a standard RFP plasma. The dynamo term includes contribution from the $m=0$ and $m=1$ tearing modes for all the axial mode numbers, n ($S=10^5$).

the oscillation of the total plasma current will decrease with S , as indicated by the relaxed state model of Sec. IV.

For both values of Lundquist number, we first evolve the plasma to a steady state in the absence of OFCD. This standard RFP plasma (at pinch parameter $\Theta=1.8$) is evolved in the presence of a constant boundary axial electric field [$E_z(a)=\text{constant}$]. It then forms the target plasma for OFCD. The radial profiles for this standard, relaxed plasma are shown in Fig. 13, which displays the parallel components of the current, electric field, and dynamo effect generated by tearing modes. As is well known, the tearing modes essentially transfer current from the core to the edge, to counter the peaking of the current by the applied electric field.

At some time during the steady-state phase of the plasma, the time-independent axial electric field is set to zero, and the oscillating poloidal and toroidal electric fields that constitute OFCD are applied. We first examine the effect on the total current and magnetic helicity. We then examine

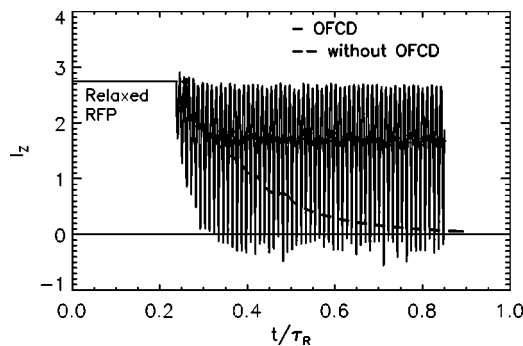


FIG. 14. Total axial current vs time. The oscillating fields $\hat{E}_z=80 \sin(\omega t)$, $\hat{E}_\theta=8 \sin(\omega t + \pi/2)$ are applied at $t=0.24\tau_R$ ($\tau_\omega=1.05 \times 10^3 \tau_A$). The bold points indicate the cycle-averaged current. The dashed line is the exponentially decaying current that occurs in the absence of OFCD [$E_z(a)$ set to zero at $t=0.24\tau_R$].

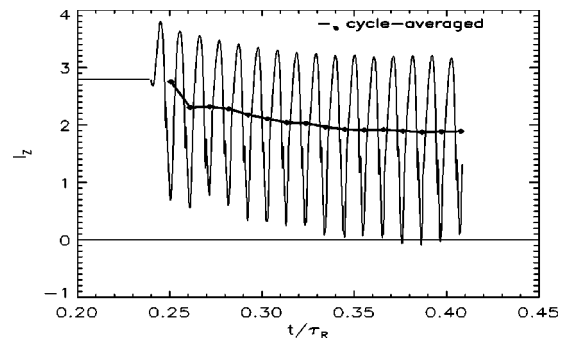


FIG. 15. Total axial plasma current vs time for $\epsilon_z=112$, $\epsilon_\theta=11$, $\tau_\omega=1.05 \times 10^3 \tau_A$, $S=10^5$. When plasma reaches quasisteady state, the cycle-averaged current, $\bar{I}_z=2$ is shown by the solid trace.

the cycle-averaged terms in Ohm's law, including the two dynamo effects—one arising from the spatially mean fields (\mathbf{V} and \mathbf{B}) oscillating at the OFCD frequency and one from the tearing fluctuations. For a most detailed analysis, we then investigate the behavior of each of the terms in Ohm's law, and the magnetic fluctuation spectrum, through an OFCD cycle. We discuss the results at $S=10^5$ in Sec. V A and $S=5 \times 10^5$ in Sec. V B.

A. $S=10^5$

The target plasma for OFCD, shown in Fig. 13, was computed with 147 radial mesh points, poloidal mode numbers $m=0-5$, and axial mode numbers $n=-21-21$. The target plasma was sustained at $\Theta=1.8$ with a helicity injection rate $\dot{K}=\phi_z v_z=50$. If the axial electric field is suddenly set to zero (at $t=0.24\tau_R$ in Fig. 14) then the current decays in a fraction of a resistive diffusion time (the dashed curve). To study OFCD, at $t=0.24\tau_R$ we impose boundary conditions $\hat{E}_z=80 \sin(\omega t)$, $\hat{E}_\theta=8 \sin(\omega t + \pi/2)$. This provides a helicity injection rate of $\hat{v}_z \hat{v}_\theta / 2\omega=35$, which is lower than the helicity injection rate of the target. As seen in Fig. 14 OFCD sustains the cycle-averaged current at about 2/3 of its initial value. However, the oscillations in the current are greater than 100%, causing the current to reverse direction.

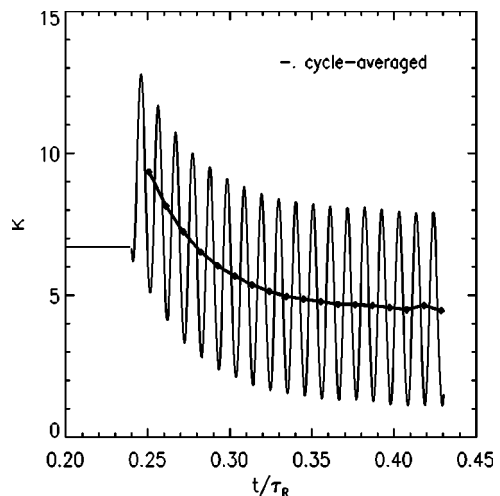


FIG. 16. Helicity vs time. The solid line with points shows the cycle-averaged helicity.

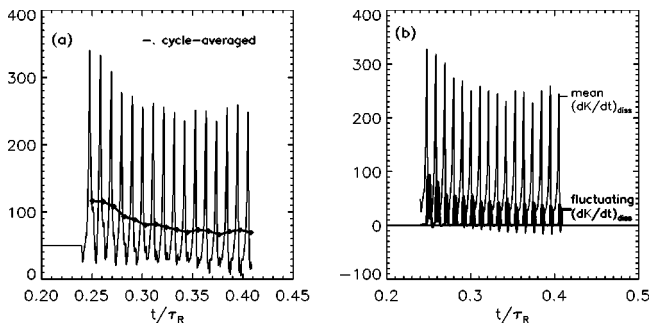


FIG. 17. (a) Total helicity dissipation rate, $\dot{K}_{diss} = \eta \int \mathbf{J} \cdot \mathbf{B} d\mathbf{v}$ vs time. The solid line is the helicity dissipation before OFCD (about 50). The bold points show the cycle-averaged total helicity dissipation rate, which at steady-state balances the OFCD helicity injection rate, $\overline{\eta \int \mathbf{J} \cdot \mathbf{B} d\mathbf{v}} \approx 67$. (b) The two terms contributing to the total helicity dissipation rate, the symmetric mean part $\eta \int \mathbf{J}_{00} \cdot \mathbf{B}_{00} d\mathbf{v}$, and the asymmetric fluctuating part $\eta \int \mathbf{J} \cdot \mathbf{B} d\mathbf{v}$ ($m, n \neq 0$) are shown. The thicker line indicates the fluctuating part.

If the OFCD helicity injection rate is increased, the cycle-averaged current increases and the relative oscillations decrease. We observe in Fig. 15 that if the OFCD helicity injection rate is doubled, then the cycle-averaged current increases by 20% and the current oscillations decrease by 10%. The cycle-averaged helicity is also seen to be sustained (Fig. 16). However, the helicity reaches a value that is less than the initial (by about 30%), despite the fact that the OFCD helicity injection rate exceeds that of the target plasma (by about 35%). This implies that the total helicity dissipation rate $\eta \int \mathbf{J} \cdot \mathbf{B} d\mathbf{v} \approx 67$, including both symmetric oscillation and asymmetric fluctuation contributions, increases with OFCD (Fig. 17). The two helicity dissipation rates are shown in Fig. 17(b). In a steady-inductive RFP surrounded by a close-fitting conducting shell, the time-averaged helicity dissipation due to the tearing fluctuations is negligible. As it is seen in Fig. 17(b) the tearing fluctuating part of the helicity dissipation increases with OFCD (shown by the thicker line), resulting in a cycle-averaged value of a few percent of the total helicity dissipation rate. Axial current (Fig. 15) decreases when the helicity dissipation due to the tearing fluctuations increases. Due to the nonlinear plasma response, both the axial current and the helicity dissipation rate are not sinusoidal in time (Figs. 15 and 17). The sudden rise of the

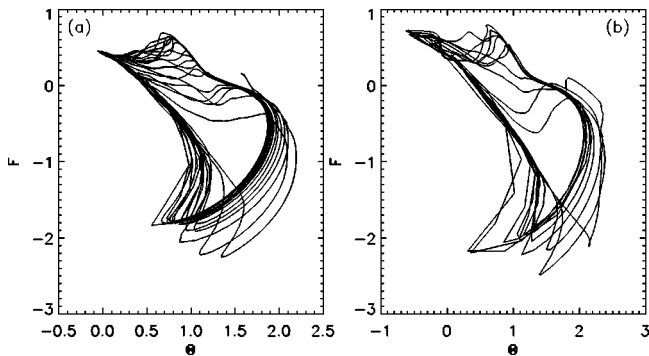


FIG. 18. $F-\Theta$ trajectories for two different periods. (a) $\tau_\omega = 1000\tau_A$, (b) $\tau_\omega = 1500\tau_A$, ($S = 10^5$), where $\tau_\omega = 2\pi/\omega$.

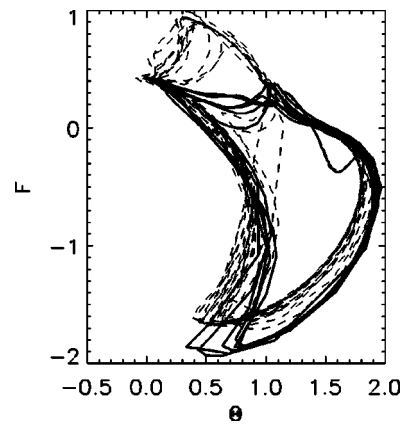


FIG. 19. $F-\Theta$ trajectories for $\varepsilon_z \varepsilon_\theta / \omega = 2.1$ (dashed) and $\varepsilon_z \varepsilon_\theta / \omega = 2.7$ (solid). The driving frequency is the same for the two cases. The toroidal field is more deeply reversed for higher helicity injection.

helicity dissipation (Fig. 17) indicates large changes in the mean profiles during a cycle.

The choice of frequency is important for efficient current drive. The frequency should be low enough that edge current can be transported by the tearing fluctuations into the plasma core, but high enough to avoid change of direction of the total plasma current through a cycle. A frequency scan for a

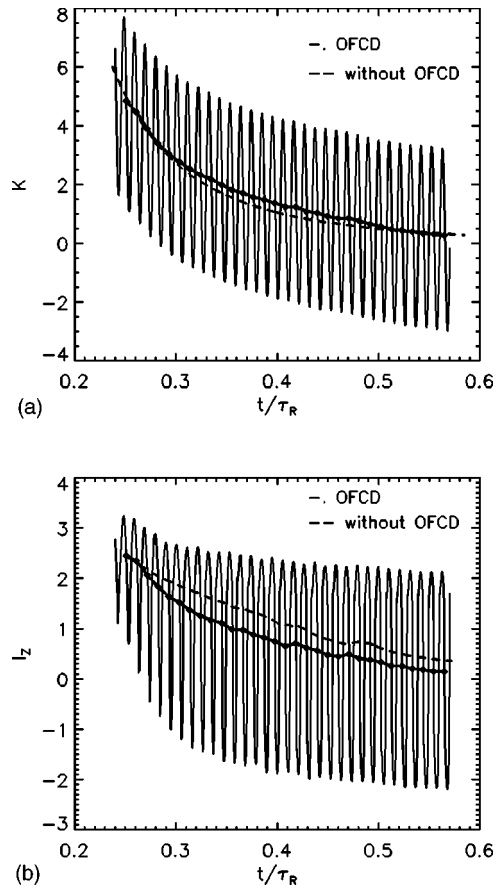


FIG. 20. (a) Helicity and (b) axial current vs time when phase between axial and poloidal oscillating fields is set to zero ($\delta = 0$). The decay of K and I_z , when ohmic axial electric field is set to zero (without OFCD) are shown with the dashed line. The bold points are the cycle-averaged quantities (with OFCD).

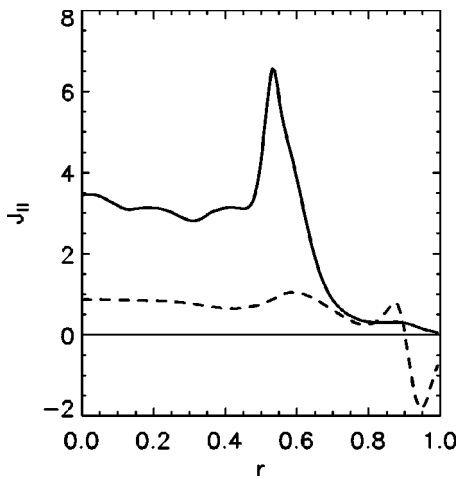


FIG. 21. Parallel current density at two different times during a cycle, at maximum (solid line) and minimum Θ (dashed line). $\varepsilon_z = 112$, $\varepsilon_\theta = 11$, and $\tau_\omega = 1.05 \times 10^3 \tau_A$.

given Lundquist number would therefore be of interest. However it is presently infeasible due to the long computational time required. At low frequency, when the driving period is much longer than the plasma relaxation time scale, the plasma current (and Θ) changes sign (Fig. 18). Whether the plasma maintains the reversal during the OFCD cycle de-

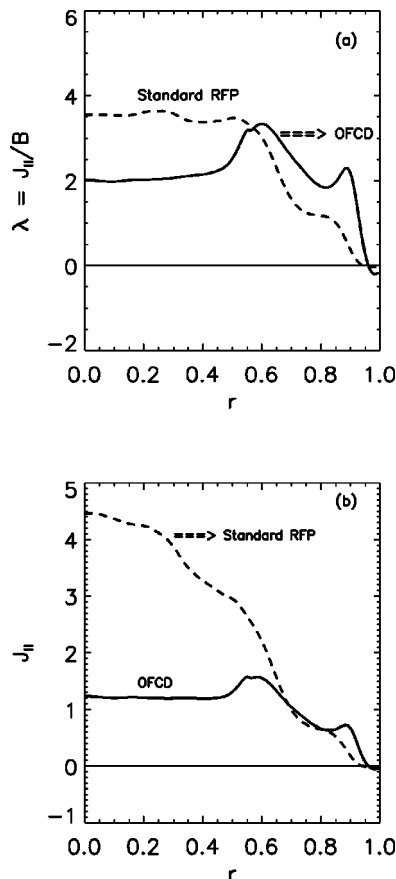


FIG. 22. (a) Cycle-averaged $\lambda = J_{\parallel}/B$ and (b) cycle-averaged parallel current density, J_{\parallel} , profile without OFCD (dashed) and with OFCD (solid). Since the total current is smaller with OFCD (see Fig. 15), J_{\parallel} is smaller as well.

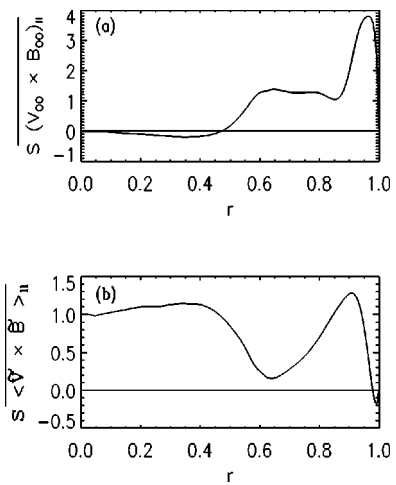


FIG. 23. Cycle-averaged dynamo terms (a) from symmetric oscillations $(\mathbf{V}_{00} \times \mathbf{B}_{00})_{\parallel}$ and (b) from the asymmetric tearing dynamo terms $\langle \mathbf{V} \times \mathbf{B} \rangle_{\parallel}$.

pends upon the ratio of the poloidal and toroidal oscillating amplitudes. At higher helicity injection rates and $\varepsilon_\theta/\varepsilon_z$ in the range of 10–15 %, the toroidal field reversal parameter, F , is less positive and plasma maintains the reversal (Fig. 19).

According to the helicity balance equation, the phase between the axial and poloidal voltages for maximal helicity injection is $\delta = \pi/2$ (Sec. I). We have also examined $\delta = 0$ and $\delta = -\pi/2$. Figure 20 shows that both the cycle-averaged helicity and the cycle-averaged current decay to zero as expected when $\delta = 0$. The dashed line in Fig. 20 shows helicity and current when the axial electric field is set to zero (no OFCD) and the solid line with bold points indicates the cycle-averaged current with OFCD with $\delta = 0$. The OFCD cycle-averaged current decays faster than the ohmic current (dashed line). The opposite phase ($\delta = -\pi/2$) leads to helicity ejection and cycle-averaged helicity and current decay more rapidly during the early cycles.

A large time variation of the parallel current density, J_{\parallel} , occurs during an OFCD cycle, shown in Fig. 21 for maximum and minimum Θ . Current density is peaked in the interior of the plasma when Θ is maximum and F is most

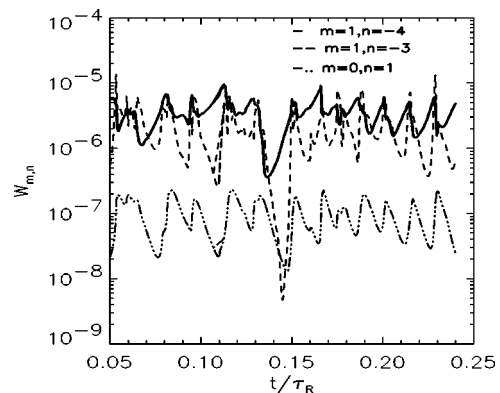


FIG. 24. Modal magnetic energy ($W_{m,n} = 1/2 \int \tilde{B}_{r(m,n)}^2 d^3r$) vs time for a standard RFP. The (1,−4) and (1,−3) modes are the most dominant tearing modes ($S = 10^5$, $R/a = 1.66$).

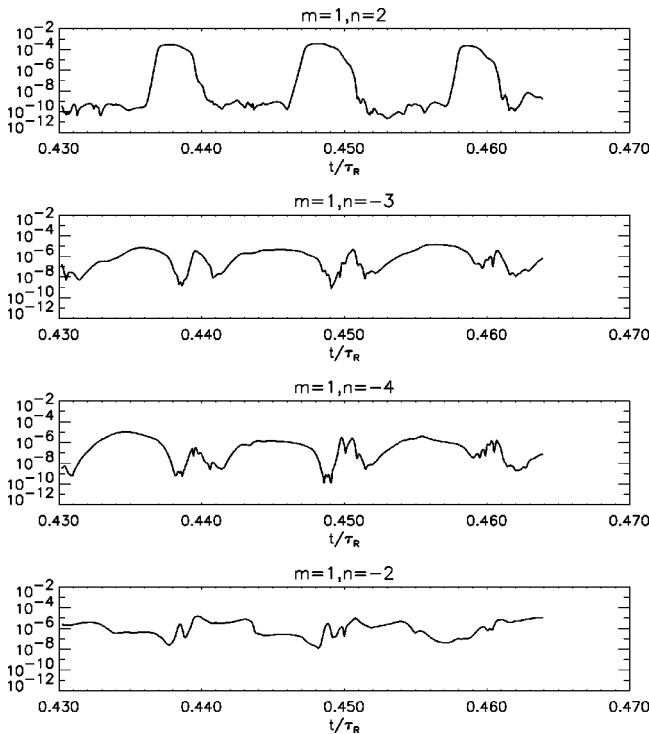


FIG. 25. Time histories of magnetic energy, $W_{m,n} = 1/2 \int \bar{B}_{r(m,n)}^2 d^3r$ for the dominant tearing modes, $(m,n) = (1,+2), (1,-3), (1,-4), (1,-2)$ in an OFCD-sustained plasma. The edge resonant mode $m=1, n=+2$, is excited by the oscillating fields and has the largest amplitude.

negative. The OFCD period is in the range of the hybrid tearing time; thus, the current penetrates to the interior of the plasma. The cycle-averaged $\lambda(r)$ profile is shown in Fig. 22. Nonzero parallel current density on axis is evidence of the penetration of edge current into the core through the tearing mode dynamo effect. The time-averaged λ and J_{\parallel} profiles of the standard RFP plasma are also shown.

The dynamics of this current relaxation can be investigated by analyzing the dynamo terms [from both the symmetric oscillations $(\mathbf{V}_{00} \times \mathbf{B}_{00})_{\parallel}$ and the tearing fluctuations $\langle \tilde{\mathbf{V}} \times \tilde{\mathbf{B}} \rangle_{\parallel}$] in the cycle-averaged parallel Ohm's law. As ex-

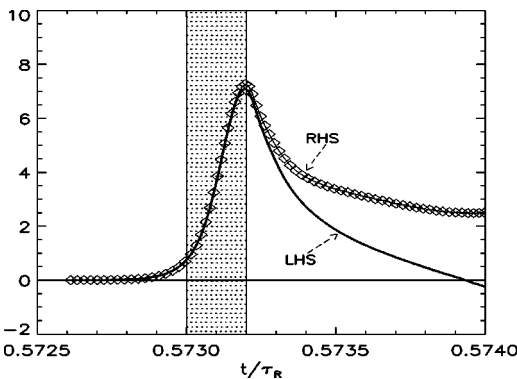


FIG. 26. The $m=1, n=+2$ energy terms (integrated over radius) of Eq. (21) vs time. The total energy (LHS) is shown by the solid line. The diamonds show the sum of the linear energy terms in the RHS. The growth period where the total energy (LHS) and linear energy (RHS) overlap, is marked by the shaded area.

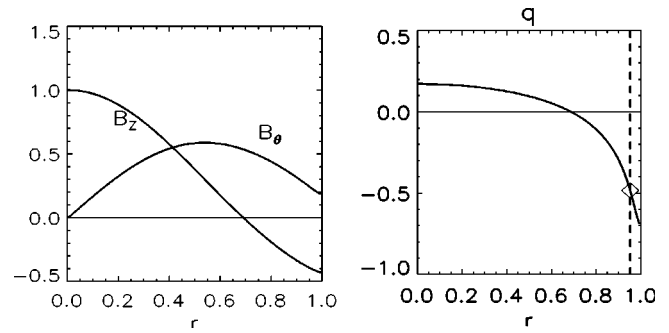


FIG. 27. Profiles of the equilibrium magnetic fields, B_z and B_{θ} , and q profile for the linear calculation of the $m=1, n=+2$ edge-resonant mode.

pected, the oscillations drive only a cycle-averaged edge current [Fig. 23(a)]. The core current is sustained by the tearing dynamo [Fig. 23(b)].

During one cycle, the plasma is driven to a state which is far from relaxed, with significant effect on fluctuations. In the standard RFP the current density is controlled by the core tearing modes, resonant within the reversal surface, with mode numbers $m=1, n=-2$ to -10 , as shown in Fig. 24. The oscillating fields of OFCD broaden the q profile and excite additional modes. Edge modes, resonant outside the reversal surface, with $m=1, n=2$, are excited, as well as additional core modes with $n=1, n=-2$, as shown in Fig. 25. The edge-resonant mode develops the largest amplitude.

The edge modes become resonant as the reversal deepens through a cycle, with F reaching -2 . To determine whether this mode is linearly unstable or nonlinearly driven we compute the linear drive terms in the equation

$$\frac{1}{2} \frac{\partial B_1^2}{\partial t} = S \mathbf{B}_1^* [(\mathbf{B}_0 \cdot \nabla) \mathbf{V}_1 - (\mathbf{V}_1 \cdot \nabla) \mathbf{B}_0] + \dots, \quad (21)$$

where the "1" subscript indicates a perturbed $m=1, n=2$ quantity and a "0" subscript indicates a mean (0,0) quantity. We compute the volume integral of the LHS and RHS of Eq. (21). We observe that during the sudden growth phase, the two terms are equal (Fig. 26). Thus, the growth of $m=1, n=2$ mode is a linear instability and nonlinearity only affects

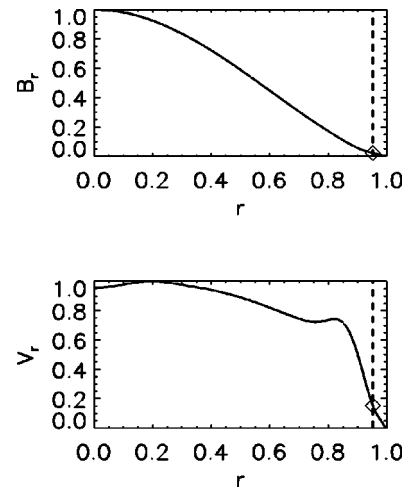


FIG. 28. Linear radial eigenfunctions of the $m=1, n=+2$ mode.

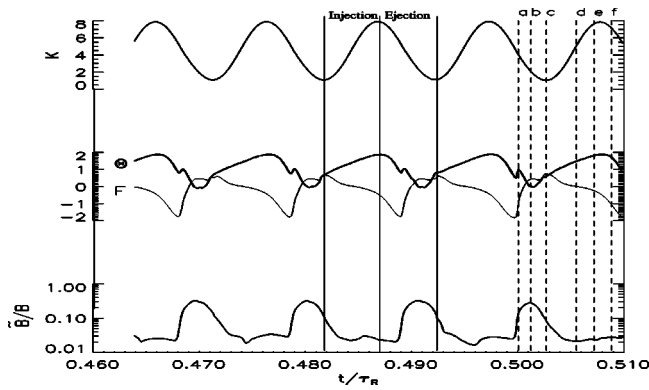


FIG. 29. Time histories of helicity K , reversal parameter F , pinch parameter Θ , and magnetic fluctuation $\tilde{\mathbf{B}}/B$ ($S=10^5$).

the saturation and damping of this mode. A linear resistive MHD stability analysis has also been performed to obtain the growth rate and spatial structure of this mode. Linear evolution of the mode is studied using the DEBS code (with all other modes suppressed). Equilibrium profiles are chosen to resemble those of the deeply reversed phase of OFCD (Fig. 27). The global eigenfunctions of the $m=1, n=+2$ mode are shown in Fig. 28. The growth rate of the mode, $\gamma\tau_A=0.1$, is in the range expected for ideal MHD instability.

The plasma experiences two phases of the magnetic fluctuations, the helicity injection and ejection phases (Fig. 29). In the helicity injection phase ($\dot{K}>0$), the total plasma current (or Θ) increases and core fluctuations transport edge current into the core. In the helicity ejection phase, Θ de-

creases, and the global edge-resonant modes suppress the current density everywhere. The λ profiles at different times during one cycle, marked by the vertical lines in Fig. 29, are shown in Fig. 30. The first three profiles (a)–(c) are during the helicity ejection phase, while (d)–(f) show the λ profiles during the injection phase. As is seen, the λ profile varies from hollow (during the ejection phase) to peaked (during the injection phase) within a cycle. Radial dynamo profiles during a cycle can provide better understanding of the current relaxation process from edge to the core region. Figure 31 illustrates the surface average dynamo term of the dominant core modes, $m=1, n=-2, -3, -4, -5$, at different times marked by the vertical lines in Fig. 29. As seen, on average the $\langle \tilde{\mathbf{V}} \times \tilde{\mathbf{B}} \rangle_{\parallel}$ term suppresses current in the core region during the ejection phase [Figs. 31(a) and 31(b)] and drives current on axis during the injection phase [Figs. 31(e) and 31(f)].

B. $S=5 \times 10^5$

Although OFCD is able to sustain the plasma current at $S=10^5$, the current oscillations are large. The relaxed state model of Sec. IV predicts that the current oscillations decrease with Lundquist number. To investigate the effect of higher Lundquist number on current oscillations and magnetic fluctuations, we have performed a computation at $S=5 \times 10^5$. We have employed higher spatial resolution (260 radial mesh points, $0 \leq m \leq 5$ and $-41 \leq n \leq 41$) to allow for more localized features that accompany higher S values. Ohmic helicity injection is replaced by OFCD at $t=0.035 \tau_R$, as shown in Fig. 32(a). The current is sustained and the

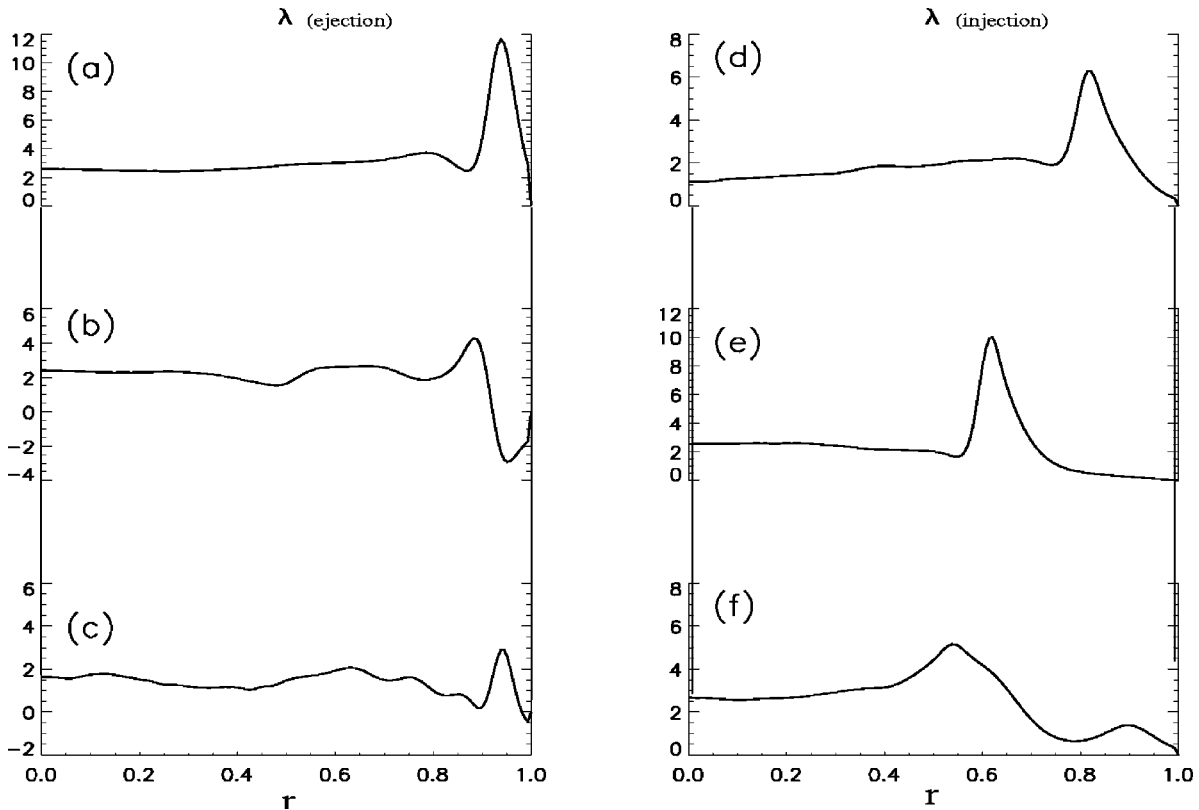


FIG. 30. λ profiles for different times during one cycle (for times marked with vertical lines in Fig. 29).

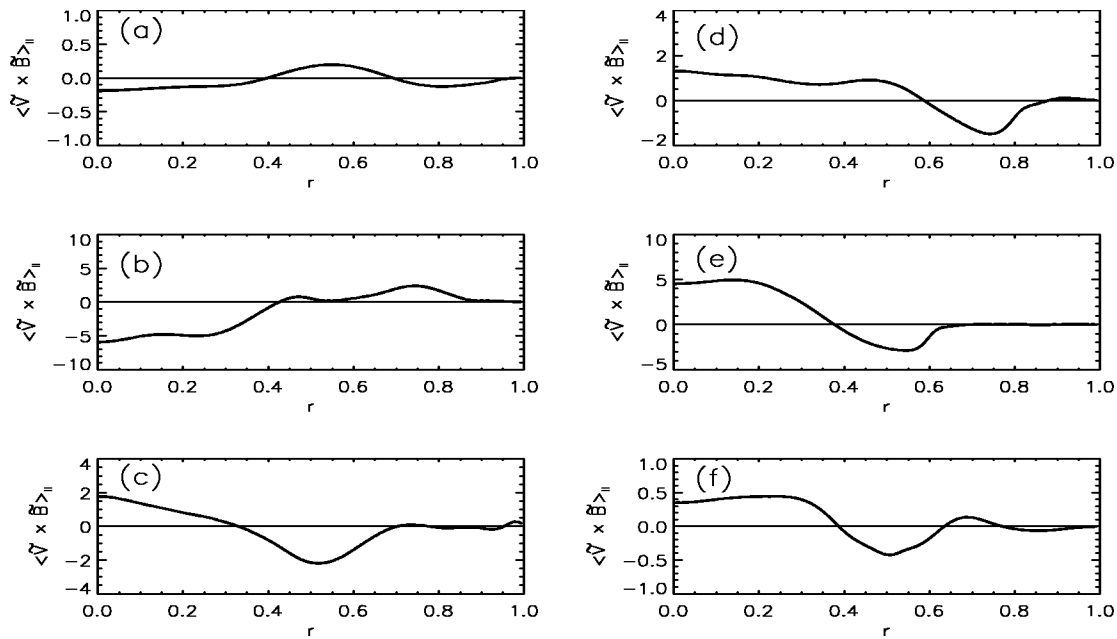


FIG. 31. Profiles of the surface-averaged dynamo, $\Sigma_{m=1,n}(\tilde{V} \times \tilde{B})_{||}$ including $n = -2, -3, -4, -5$, at different times during one cycle (times marked with vertical lines in Fig. 29).

oscillations are indeed reduced by about 50% relative to $S = 10^5$. The corresponding $F - \Theta$ trajectory is shown in Fig. 32(b), where it is seen that the plasma maintains reversal for most of the cycle.

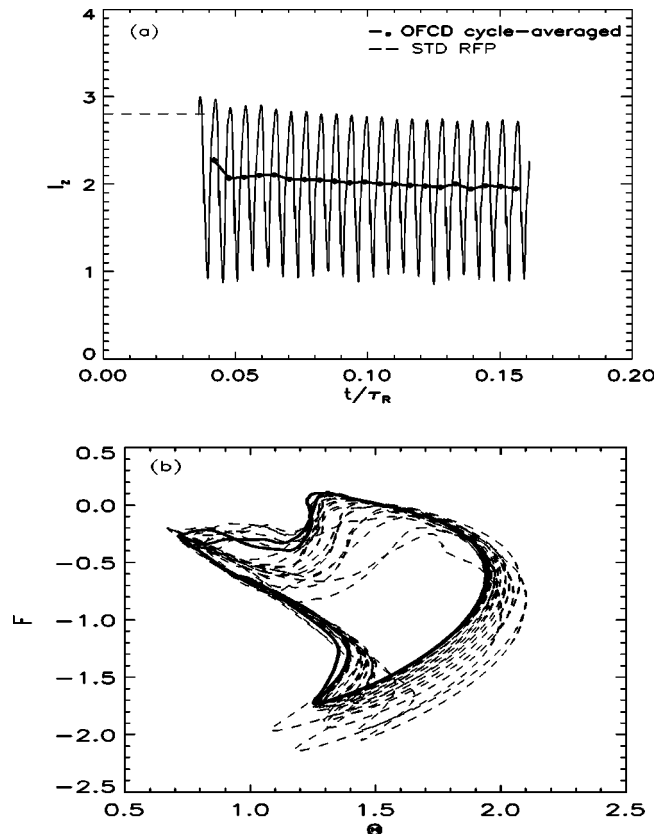


FIG. 32. (a) Toroidal plasma current I_z , and (b) $F - \Theta$ trajectory for OFCD-sustained plasma at $S = 5 \times 10^5$ ($\varepsilon_z = 140$, $\varepsilon_\theta = 16$, and $\tau_\omega = 2.85 \times 10^3 \tau_A$). The $F - \Theta$ limit cycle is shown by the solid curve.

The cycle-averaged λ profile is shown in Fig. 33. For the same helicity injection rate, the cycle-averaged parallel current density on axis is higher than the $S = 10^5$ case, indicating that current penetrates more effectively into the plasma core at higher S . Similar to the $S = 10^5$ case, there are two phases, the helicity injection (current drive phase) and helicity ejection (current reversal phase). In the helicity injection phase, the positive dynamo term from the core tearing fluctuations, transfers the edge current into the core. Because of the excitation of the edge-resonant modes, magnetic fluctuations level are enhanced (about the same level of $S = 10^5$ case) during the ejection phase. The λ profiles during the injection and ejection phases are shown in Fig. 34. This profile varies from hollow (during the ejection phase) to peaked (during the injection phase) within a cycle.

Figures 35(a)–35(d) illustrates the $m = 1$ magnetic energy spectrum, at different times during the OFCD cycle. The corresponding q profiles are shown in Figs. 36(a)–36(d),

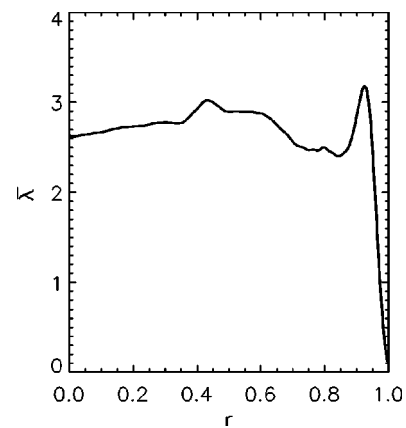


FIG. 33. Radial profile of cycle averaged λ ($S = 5 \times 10^5$).

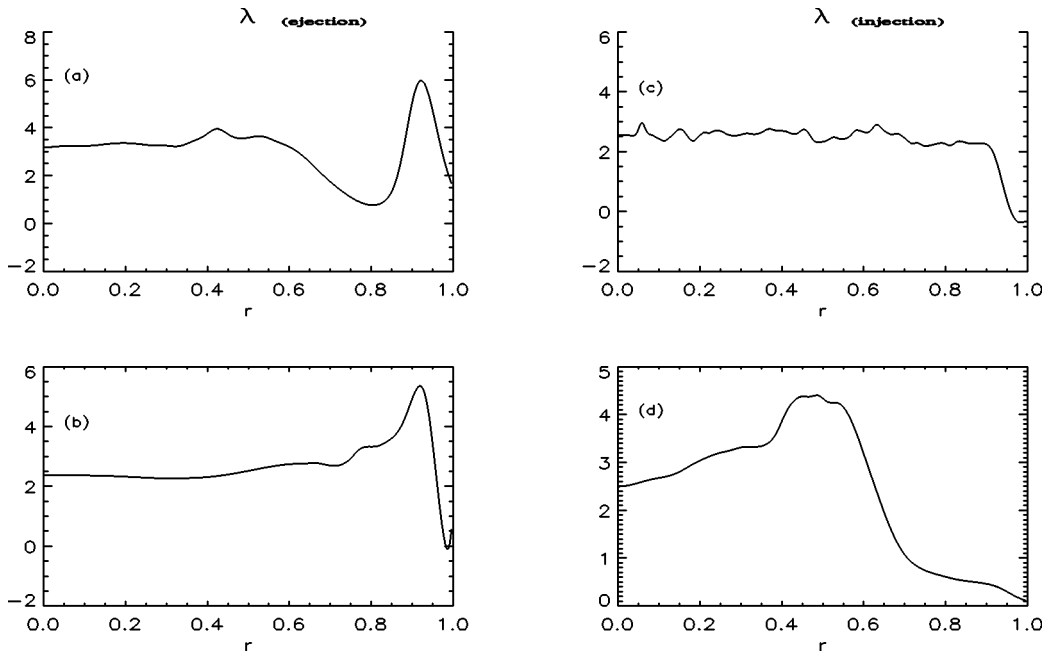


FIG. 34. λ profiles at four different times during OFCD cycle (ejection and injection phases), $S=5 \times 10^5$.

including the cycle-averaged q profile (shown by the thicker line) for comparison. The dominant core modes $m=1, n = -3, -4, -5, -6$ can be seen in Fig. 35(a) with the magnetic fluctuation level about 0.1–2%. This spectrum is the typical spectrum during the maximum current drive, maximum Θ , and is similar to the standard inductive RFP spec-

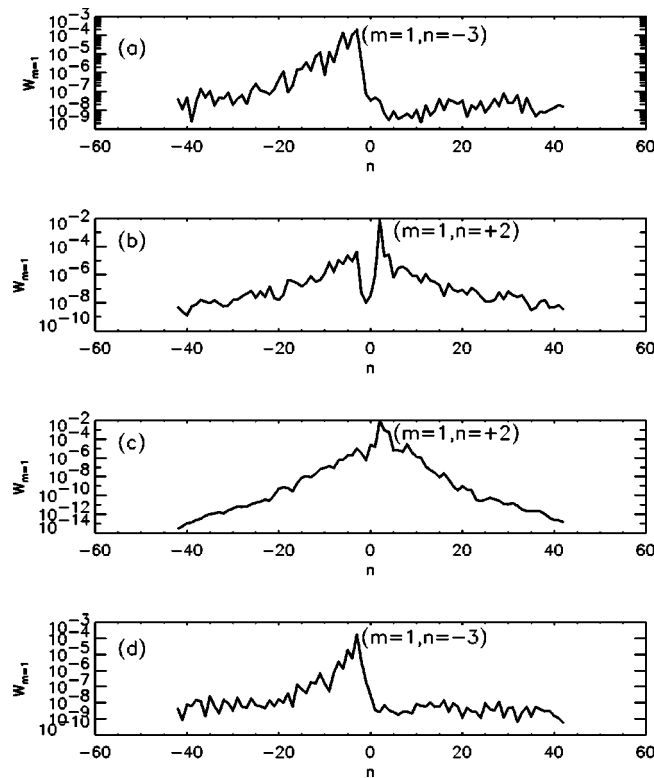


FIG. 35. The evolution of magnetic energy $W_{m=1,n} = 1/2 \int B_{r,(m=1,n)}^2 d^3r$, spectrum during OFCD cycle ($S=5 \times 10^5$). The dominant (m,n) modes have also been specified.

trum. The q profile at this time is shown in Fig. 36(a). As discussed earlier, when the plasma reversal starts to deepen, edge-resonant modes become linearly unstable and the dominant modes move toward the positive part of the spectrum. The q profile on the edge becomes more negative [Fig. 36(b)]. The linearly growing $m=1, n = +2$ mode is seen in Fig. 35(b). This figure shows the magnetic spectrum during the growth of edge-resonant mode fluctuations. At this time the $m=1, n = +2$ fluctuation level is about 10% and the core mode ($m=1, n = -3, -4, -5, -6$) fluctuation level is about 0.1–1%. It can also be seen in Fig. 35(c) that the amplitudes of other edge-resonant modes $m=1, n = +3, +4$ start to increase to higher values (1–5%) during the peak of the \bar{B}/B . The q profile for this spectrum is broader both on axis and on the edge [Fig. 36(c)]. The spectrum after the decay of

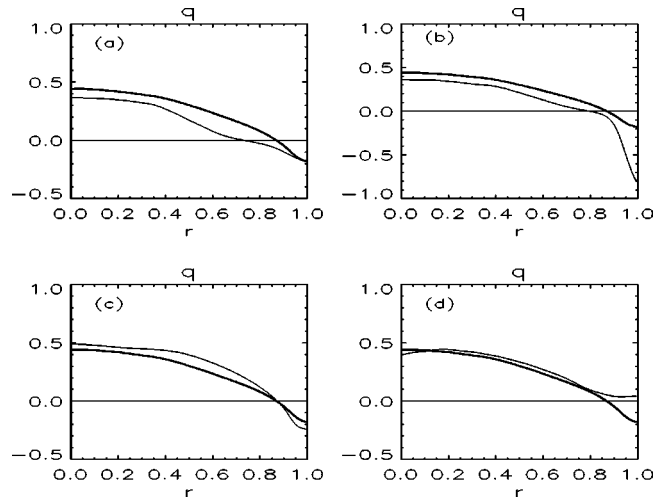


FIG. 36. (a)–(d) are the q profiles for the spectrums (a)–(d) in Fig. 35, respectively. The thicker profile is the cycle-averaged q profile.

edge-resonant modes begins to return to the typical standard RFP spectrum with the core dominant mode $m = 1$, $n = -3$. Figures 35(d) and 36(d) show the spectrum and the q profile at a time during the injection phase.

VI. SUMMARY AND DISCUSSION

We have investigated the full nonlinear dynamics of OFCD, a form of ac helicity injection, using 3D nonlinear MHD computation. Three-dimensional plasma fluctuations and instabilities in large part determine the effectiveness of OFCD and its influence on confinement. The full dynamics are compared with results from 1D models, previously investigated. In a classical 1D plasma, devoid of nonaxisymmetric fluctuations, OFCD generates a steady-state current confined to within a resistive skin depth of the plasma surface. The current is generated by the cycle-averaged dynamo-like $(\mathbf{V}_{00} \times \mathbf{B}_{00})_{\parallel}$ effect from the axisymmetric velocity and magnetic field oscillations. We also find that, at large amplitude of the oscillating voltages, transient fields are generated that persist for about a resistive diffusion time.

The effect of the fluctuations, or magnetic relaxation, has been incorporated in a 1D model by assuming that the J_{\parallel}/B profile maintains a preferred radial shape. This model reveals the dependence of OFCD dynamics on key parameters such as Lundquist number and frequency. Generally, these 1D results are consistent with those obtained from 3D computation. Of particular interest is that the oscillation in the total toroidal plasma current decreases with Lundquist number, S .

The edge current driven classically, excites plasma fluctuations which then drive current in the core through the dynamo effect that arises from nonaxisymmetric velocity and magnetic fluctuations. That is, magnetic relaxation causes the current to penetrate to the core. This physics is captured through 3D MHD computation. We find that OFCD indeed can sustain the plasma current steadily in the absence of a dc electric field. There are two causes for concern for the technique. First, the symmetric plasma quantities, such as the toroidal current, experience very large oscillations. For example, at $S = 10^5$ the current oscillates by 100%, a value likely unacceptable in an experimental plasma. However, we find that the current oscillation decreases to about 50% at $S = 5 \times 10^5$, consistent with the prediction of the 1D relaxed state model that oscillations scale as $S^{-1/4}$. Thus, at the higher S values of experiments or a reactor, the current oscillation may be acceptably small. We have also optimized OFCD with regard to frequency and other parameters. As expected, the optimum frequency is one that is sufficiently low to permit relaxation to occur and sufficiently high that the oscillation in the total current is minimized.

Second, plasma fluctuations (and transport) can be affected by OFCD. The OFCD dynamics is complex. The profiles of the mean fields (such as J_{\parallel}/B) and the fluctuations vary widely throughout a cycle. The J_{\parallel}/B profile varies from hollow to peaked within a cycle. The profiles are such that the helicity dissipation is higher than for conventional current sustainment by a dc toroidal electric field. Hence, the helicity injection rate for an OFCD-sustained plasma is

greater than that for standard Ohmic plasmas. We identify two parts of the OFCD cycle. During the helicity injection phase, the current density profile peaks and the tearing mode dynamo drives current in the core (transporting current from edge to the core). The fluctuation level is roughly equal to that of the standard RFP. During the helicity ejection phase, new global modes appear that are resonant at the extreme plasma edge. These modes produce a "dynamo" effect that suppresses current everywhere. A linear stability analysis shows that these modes are unstable in plasmas with strong field reversal (large, negative toroidal magnetic field at the plasma surface). The instability is suppressed in high S plasmas where the reversal is weak. Clearly, investigations at yet higher S values, beyond the scope of the present computation, is needed.

An area for further study is optimization of OFCD with the aim of providing current drive with minimal tearing fluctuations. For example, is a steady-state RFP possible without a core plasma current and the attendant need for core fluctuations? Another area of future research is the use of OFCD for current profile control, rather than sustainment.

ACKNOWLEDGMENT

We are grateful to Dalton Schnack for useful discussions.

- ¹See National Technical Information Service Document No. DE82008957 (Los Alamos National Laboratory Report LA-8944-C by M. K. Bevir and J. W. Gray, 1981). Copies may be ordered from the National Technical Information Service, Springfield, VA.
- ²T. H. Jensen and M. S. Chu, *Phys. Fluids* **27**, 2881 (1984).
- ³M. K. Bevir, C. G. Gimblett, and G. Miller, *Phys. Fluids* **28**, 1826 (1985).
- ⁴T. R. Jarboe, I. Henins, A. R. Sherwood, C. W. Barnes, and H. W. Hoida, *Phys. Rev. Lett.* **51**, 39 (1983).
- ⁵M. Ono, G. J. Greene, D. Darrow, C. Forest, H. Park, and T. H. Stix, *Phys. Rev. Lett.* **59**, 2165 (1987).
- ⁶T. R. Jarboe, M. A. Bohnet, A. T. Mattick, B. A. Nelson, and D. J. Orvis, *Phys. Plasmas* **5**, 1807 (1998).
- ⁷S. Kaye, M. Ono, Y. K. M. Peng *et al.*, *Fusion Technol.* **36**, 16 (1999).
- ⁸K. F. Schoenberg, J. C. Ingraham, C. P. Munson *et al.*, *Phys. Fluids* **31**, 2285 (1988).
- ⁹J. B. Taylor, *Phys. Rev. Lett.* **33**, 1139 (1974).
- ¹⁰K. F. Schoenberg, R. F. Gribble, and D. A. Baker, *J. Appl. Phys.* **56**, 2519 (1984).
- ¹¹H. R. Strauss and D. S. Harned, *Phys. Fluids* **30**, 164 (1987).
- ¹²D. S. Harned, D. D. Schnack, H. R. Strauss, and R. A. Nebel, *Phys. Fluids* **31**, 1979 (1988).
- ¹³C. R. Sovinec, J. M. Finn, and D. del-Castillo-Negrete, *Phys. Plasmas* **8**, 475 (2001).
- ¹⁴C. R. Sovinec and S. C. Prager, *Phys. Plasmas* **3**, 1038 (1996).
- ¹⁵Z. Yoshida and A. Hasegawa, *Phys. Fluids B* **3**, 3059 (1991).
- ¹⁶R. W. Moses, R. A. Gerwin, and K. F. Schoenberg, *Phys. Plasmas* **8**, 4839 (2001).
- ¹⁷D. D. Schnack, D. C. Barnes, Z. Mikic, D. S. Harned, and E. J. Caramana, *J. Comput. Phys.* **70**, 330 (1987).
- ¹⁸P. M. Bellan, *Phys. Rev. Lett.* **54**, 1381 (1985).
- ¹⁹F. Najmabadi, R. W. Conn, R. A. Krakowski *et al.*, *Fusion Eng. Des.* **23**, 69 (1993).
- ²⁰M. R. Stoneking, J. T. Chapman, D. J. Den Hartog, S. C. Prager, and J. S. Sarff, *Phys. Plasmas* **5**, 1004 (1998).
- ²¹C. R. Sovinec, Ph.D. thesis, University of Wisconsin, Madison, 1995.
- ²²S. Cappello and D. Biskamp, *Nucl. Fusion* **36**, 571 (1996).
- ²³Y. L. Ho, D. D. Schnack, P. Nordlund, S. Mazur, H.-E. Satherblom, J. Scheffel, and J. R. Drake, *Phys. Plasmas* **2**, 3407 (1995).